EPJ D
Atomic, Molecular, Optical and Plasma Physics
EPJ.org
your physics journal

Eur. Phys. J. D (2014) 68: 183 DOI: 10.1140/epjd/e2014-40796-0

Low-energy positron scattering from gas-phase uracil

Jan Franz, Franco A. Gianturco and Isabella Baccarelli

edp sciences
Società Italiana di Fisica
Springer

Eur. Phys. J. D (2014) 68: 183
DOI: 10.1140/epjd/e2014-40796-0

THE EUROPEAN PHYSICAL JOURNAL D

Regular Article

Low-energy positron scattering from gas-phase uracil*

Jan Franz[1,2,a], Franco A. Gianturco[3,4], and Isabella Baccarelli[5]

[1] Department of Atomic, Molecular and Optical Physics, Faculty of Applied Physics and Mathematics, Gdansk University of Technology, ul. Narutowicza 11/12, 80-233 Gdansk, Poland
[2] Interdisciplinary Laboratory for Computational Science, FBK-CMM, via Sommarive 18, 38123 Povo, Trento, Italy
[3] Intitute of Ion Physics, The University of Innsbruck, Technikerstr. 25, 6020 Innsbruck, Austria
[4] Scuola Normale Superiore, Piazza dei Cavalieri 7, 56126 Pisa, Italy
[5] CINECA, Via de Tizii 6, 00185 Rome, Italy

Received 14 December 2013 / Received in final form 25 March 2014
Published online 1 July 2014

Abstract. Quantum scattering calculations are presented for the interaction of low energy positrons with the uracil molecule, an important component of biological systems. The rotational elastic and inelastic cross sections and vibrational inelastic cross sections are reported and compared with existing experiments, indicating a general trend of the cross sections different from the experimental findings and in line with what should be expected from the behavior of the total cross sections in similar polar targets. Some specific considerations can be drawn on the reliability of existing experiments, as to their size vis-à-vis to the computed integral cross sections over the same range of energies.

1 Introduction

The damaging effects on biological systems of ionizing radiation has been known for a long time, as it is by now an accepted fact that high-energy particles (α, β, γ and possible atomic ions) are capable of ionizing cell components along the track of radiation, thus leading to various dissociation channels and to the formation of damaging radical species [1,2]. One additional piece of information from recent studies has also been the fact that about one third of the damage actually comes from energy that is transferred to the DNA cell structures, and to the nearby molecules bound to them, while the remaining two thirds of the destructive action comes from the secondary electrons extracted by the primary radiation from the molecular environment, thereby leading to single and double strand breaks and to other lethal, mutagenic DNA and RNA lesions caused by such secondary electrons [3,4].

The above findings on secondary electron effects have triggered a great deal of studies, both experimentally and theoretically, on the behavior of DNA and its components under the exposure to low-energy electron beams, following both the shear size of the relevant cross sections and the ensuring fragmentation patterns as indications to final DNA irreversible damage [5–8]. With the same token, people have also become interested in comparing such novel findings with the corresponding behavior on biosystems under the low-energy scattering of the electron's antiparticle, the positron, whose low-energy interactions with polyatomic molecules have also created a great deal of interest in recent years (for a comprehensive discussion see the recent Refs. [9,10]) since the positive projectile indeed interacts with the electro-nuclear network of the molecular targets essentially via the same fundamental forces. However the additional channels of positron annihilation and positronium (Ps) formation also provide new and intriguing possibilities among the scattering channels (for some theoretical work treating annihilation see e.g. [11–13] and for some recent reviews see e.g. [14,15]).

In the present work we have therefore taken up one of the most popular biological molecules that have been studied with electron scattering experiments and theory, the uracil molecule, and have examined the behavior of its differential and integral cross sections by low-energy scattering of a beam of positrons: for this initial study we have included rotationally elastic and inelastic channels and vibrationally elastic channels. In current experimental setups the sum of the cross sections for these channels is measured, because due to the limited energy resolution these channels cannot be distinguished form each other, see e.g. [16,17]. In this study the annihilation, Ps-formation and ionization channels have not been considered in our computational treatment. Experimentally these channels can be distinguished very clearly

* Contribution to the Topical Issue "Electron and Positron Induced Processes", edited by Michael Brunger, Radu Campeanu, Masamitsu Hoshino, Oddur Ingólfsson, Paulo Limão-Vieira, Nigel Mason, Yasuyuki Nagashima and Hajime Tanuma.

[a] e-mail: j.franz@ucl.ac.uk

from rotationally elastic and inelastic channels and vibrationally inelastic channels.

Furthermore Ps-formation and ionization are reactive channels and are difficult to describe with the model potential based approach used in this study. Gianturco and Melissa have employed in earlier work an optical model potential to describe the Ps-formation channel in positron scattering from neutral atoms [18,19] and atomic ions [20]. This method is however difficult to reliably be included within our present approach, so that we have, for the time being, disregarded its implementation for polyatomic molecular targets. Another possibility is to introduce a complex absorbing potential, which describes both channels, Ps-formation and ionization, as done by Baluja and Jain [21] and Reid and Wadehra [22,23]. One disadvantage of this approach is that the channels for Ps-formation and ionization cannot be distinguished and that additional empirical parameters are introduced. Reid and Wadehra [22,23] needed to introduce an empirical quantity Δ, which they identify with the threshold energy for Ps-formation. This choice reproduces the sum of Ps-formation and ionization cross sections near the Ps-formation threshold, but decays too fast at higher energies, and therefore Chiari et al. [24] tried instead to use an energy-dependent threshold parameter in order to correct for this behavior. This corrects the high-energy shape of the cross-section but destroys the non-empirical character of the original approach.

The couplings between open channels, like Ps-formation, electronic-excitation or ionization, usually will give structure in the elastic cross section on either side of each threshold for opening a new inelastic channel, see e.g. Charlton and Humberston [9] for a detailed discussion. The effects on the structure of the rotationally and vibrationally elastic and inelastic cross sections can be expected to be much smaller than the uncertainties originating from other aspects of our model. Therefore it should be a valid assumption to neglect the effects of these channels onto the presented cross sections.

The threshold for positronium formation is given by $E_{\mathrm{Ps}} = E_{\mathrm{ion}} - 6.8$ eV [9]. Experiments (see e.g. Denifl et al. [25]) and theory (see e.g. Wetmore el al. [26]) place the vertical ionization energy at roughly $E_{\mathrm{ion}} \approx 9.5$ eV, which gives $E_{\mathrm{Ps}} \approx 2.7$ eV. Positron-electron annihilation is possible at all collision energies. In the absence of resonances the annihilation channel is usually only weakly coupled to the elastic and inelastic channels and often treated uncoupled as an expectation value of the scattering wave function (see e.g. Chap. 4.2 in Charlton and Humberston [9] and in Humberston et al. [27]). We therefore also neglect the influence of annihilation on the presented cross sections.

The following section briefly reports on our theoretical and computational model, described in greater detail elsewhere (see e.g. [28]), while Section 3 deals with our present results. Section 4 finally summarizes our conclusions, where a detailed comparison is also reported with the few available experimental data on our title molecule.

2 Theoretical and computational methods

2.1 Scattering equations

In order to obtain the scattering cross sections for polyatomic molecules, we need to solve the Schrödinger equation of the total system

$$(H - E)\Psi = 0 \tag{1}$$

at the total energy E, for the corresponding wavefunction Ψ. Here H is the total Hamiltonian given by

$$H = H_{\mathrm{mol}} + K + V, \tag{2}$$

where H_{mol}, K and V represent the operators of the molecular Hamiltonian, kinetic energy for the scattered positron and the interaction potential between the incident positron and the target molecule, respectively. The H_{mol} further consists, in general, of the rotational and vibrational parts

$$H_{\mathrm{mol}} = H_{\mathrm{rot}} + H_{\mathrm{vib}}, \tag{3}$$

whereby we exclude, at the collision energies considered, electronic excitations, ionization and the Ps formation channels.

The total wavefunction Ψ is described in the body-fixed (BF) reference frame, in which the z axis is taken along the direction of the main molecular axis and is expanded around a single-centre (SCE) as

$$\Psi(\mathbf{r}_1 \ldots \mathbf{r}_Z, \mathbf{r}_p|\mathbf{R}) = \Psi_{\mathrm{mol}}(\mathbf{r}_1 \ldots \mathbf{r}_Z|\mathbf{R})\varphi(\mathbf{r}_p|\mathbf{R}), \tag{4}$$

where

$$\varphi(\mathbf{r_p}|\mathbf{R}) = \sum_{l\pi\mu h} r_p^{-1} u_{lh}^{\pi\mu}(r_p|\mathbf{R}) X_{hl}^{\pi\mu}(\hat{\mathbf{r}}_p). \tag{5}$$

In equation (4), $\mathbf{r_i}$ represents the position vector of the ith electron among the Z bound electrons in the target, taken from the centre of mass. Ψ_{mol} is the electronic wavefunction for the molecular target at the nuclear geometry $\mathbf{R}$. The continuum function $\varphi(\mathbf{r_p}|\mathbf{R})$ refers to the wavefunction of the scattered positron under the full action of the field created by the molecular electrons and by their response to the impinging positron as described in reference [28]. Each $u_{lh}^{\pi\mu}$ is the radial part of the wavefunction for the incident particle and the $X_{hl}^{\pi\mu}$ are the symmetry-adapted angular basis functions (for more detailed informations see e.g. [29]). The suffix π stands for the irreducible representation (IR), μ distinguishes the components of the basis, if its dimension is greater than one and h does the same within the same set with angular momentum quantum number l.

We can now assume that the target molecule can be kept fixed during the collision, since the molecular rotations and vibrations are often slower when compared with the velocity of the impinging positrons considered in the present study. This is called the fixed-nuclei (FN) approximation [30] that ignores the molecular term of H_{mol} in

equation (2) and fixes the values of all **R** at their equilibrium locations in the target molecule. To solve the Schrödinger equation in the FN approximation, we make use of the body-fixed (BF) system rather than the space-fixed (SF) frame of reference, because a formulation in the former can be simpler, both conceptually and computationally. The two systems are related through a frame transformation scheme given, for example, by Chang and Fano [30].

After substituting equation (4) into (1) under the FN approximation, we obtain a set of coupled differential equations for u_{lv} where, for simplicity, v represents $(\pi\mu h)$ collectively:

$$\left\{\frac{d^2}{dr_p^2} - \frac{l(l+1)}{r_p^2} + k^2\right\} u_{lv}(r_p|\mathbf{R}) = 2\sum_{l'v'}\langle lv|\mathbf{V}|l'v'\rangle u_{l'v'}(r_p|\mathbf{R}) \quad (6)$$

with

$$\langle lv|\mathbf{V}|l'v'\rangle = \int d\hat{r}_p X^*_{lv}(\hat{r}_p) V(r_p|\mathbf{R}) X_{l'v'}(\hat{r}_p). \quad (7)$$

When solving equation (6) under the boundary conditions that the asymptotic form of u_{lv} is represented by a sum containing outgoing spherical Bessel- and Neumann functions we obtain the corresponding S-matrix elements, $S^{lv}_{l'v'}$. The actual numerical procedure we have employed to solve that equation is given in detail in references [31,32].

The integral cross section (ICS) for the elastic scattering in the BF frame is given by

$$\sigma_{cc} = \frac{\pi}{k^2}\sum_{lv}\sum_{l'v'}\left|T^{lv}_{l'v'}\right|^2, \quad (8)$$

where the index cc indicates the close-coupling approach.

The **T**-matrix is defined as a function of the **S** and **K**-matrices,

$$\mathbf{T} = 1 - \mathbf{S} \quad (9)$$

$$= 1 - (1 - i\mathbf{K})\cdot(1 + i\mathbf{K})^{-1}. \quad (10)$$

The differential cross section diverges in the forward direction in the presence of a molecular dipole moment, because of the long-range interaction between the positron and the molecular dipole moment. This is particularly important for the present molecule, where the permanent dipole value is fairly large and known to be around 4 Debye [33–35]. This problem can be solved by applying the following closure formula for the differential cross section [36]:

$$\frac{d\sigma}{d\Omega}(J_\tau \to J'_{\tau'}) = \frac{d\sigma^B_{rd}}{d\Omega}(J_\tau \to J'_{\tau'}) + \sum_L \left(A_L - A^B_L\right) P_L(\cos\theta), \quad (11)$$

where J_τ and $J'_{\tau'}$ denote the initial and final rotational level, respectively. The first quantity on the right hand side is the differential cross section for a rotating dipole using the first Born approximation. The $P_L(\cos\theta)$ are the Legendre functions. The coefficients A_L are computed from the **K**-matrices, which are obtained by solving the close-coupling equations. The coefficients A^B_L are computed from the **K**-matrices using the first Born approximation for the dipole potential. Explicit formulas for A_L and A^B_L are given in Gianturco and Jain [29]. The final differential cross section is obtained by summation over the the different initial and final rotational levels

$$\frac{d\sigma_{\rm rot}}{d\Omega} = \sum_{J\tau J'\tau'} w_{J_\tau}\frac{d\sigma}{d\Omega}(J_\tau \to J'_{\tau'}), \quad (12)$$

where w_{J_τ} is the relative occupation of the initial rotational level $J\tau$. Here we are considering only the case with initial rotational level $J_\tau = 0_0$, corresponding to a temperature of 0 K. In our previous study on pyrimidine [37] we have shown that the cross section changes less than 5 percent by changing the temperature from 0 to 1000 K. We define the partial differential cross section for the transition between the rotational levels J and J' by

$$\frac{d\sigma^{\rm rot}_{JJ'}}{d\Omega} = \sum_{\tau\tau'}\frac{d\sigma}{d\Omega}(J_\tau \to J'_{\tau'}), \quad (13)$$

in which we sum over all initial and final sub-levels τ and τ'. In the following we use the notation $\frac{d\sigma_{\rm elas}}{d\Omega}$ for the rotationally elastic cross section, i.e.

$$\frac{d\sigma_{\rm elas}}{d\Omega} = \frac{d\sigma}{d\Omega}(0_0 \to 0_0). \quad (14)$$

It should be noted that the above sum $\frac{d\sigma_{\rm rot}}{d\Omega}$ includes the rotationally elastic cross section.

The integral cross section for the rotational transition from the initial state J_τ to the final state $J'_{\tau'}$ can be computed in the SF frame as

$$\sigma^{\rm rot}_{(J_\tau \to J'_{\tau'})} = \int \frac{d\sigma}{d\Omega}(J_\tau \to J'_{\tau'})\, d\Omega. \quad (15)$$

The integral cross section for the rotational transition between the two rotational states J and J' is given by

$$\sigma^{\rm rot}_{JJ'} = \sum_{\tau\tau'}\int \frac{d\sigma}{d\Omega}(J_\tau \to J'_{\tau'})\, d\Omega \quad (16)$$

$$= \sum_{\tau\tau'}\sigma^{\rm rot}_{(J_\tau \to J'_{\tau'})}, \quad (17)$$

where again we sum over all initial and final sub-levels τ and τ'. The rotationally elastic integral cross section is given by

$$\sigma_{\rm elas} = \sigma^{\rm rot}_{(0_0 \to 0_0)}. \quad (18)$$

The sum of rotationally elastic and inelastic cross sections is given by

$$\sigma_{\rm rot} = \sum_{JJ'}\sigma^{\rm rot}_{JJ'}. \quad (19)$$

For transitions from the ground state with $J = 0$ this sum is already converged by including terms up to $J' = 4$. Alternatively this cross section can be computed as

$$\sigma_{\rm rot}^{\rm closure} = \sigma_{rd}^{B} + \sigma_{cc} - \sigma_{fd}^{B}, \tag{20}$$

as discussed by Sanna and Gianturco [36]. Here σ_{rd}^{B} is the integral cross section for a rotating dipole in the Born approximation. σ_{cc} is the integral cross section obtained by solving the close-coupling equations in the FN-approximation and σ_{fd}^{B} is the integral cross section for a fixed dipole. In our computations the two expressions $\sigma_{\rm rot}$ and $\sigma_{\rm rot}^{\rm closure}$ coincide by more than 8 significant figures, which is a good sign that all quantities are numerically converged.

2.2 The DFT modelling of correlation and polarization

The interaction between the positron and the molecular nuclei and electrons is specified by the total interaction potential

$$V_{\rm tot}(\mathbf{r}_p|\mathbf{R}) = V_{\rm st}(\mathbf{r}_p|\mathbf{R}) + V_{\rm pcp}(\mathbf{r}_p|\mathbf{R}), \tag{21}$$

which is the sum of the static potential $V_{\rm st}$ and the correlation-polarization potential $V_{\rm pcp}$. The static potential $V_{\rm st}$ is the exact electro-static interaction potential between the positron and the nuclei and electrons in the molecule. The correlation-polarization potential is modeled by the potential [32]

$$V_{\rm pcp}(\mathbf{r}_p|\mathbf{R}) = \begin{cases} V_{\rm corr}(\mathbf{r}_p|\mathbf{R}) \text{ for } r_p \le r_c \\ V_{\rm pol}(\mathbf{r}_p|\mathbf{R}) \text{ for } r_p > r_c. \end{cases} \tag{22}$$

Here $V_{\rm corr}$ and $V_{\rm pol}$ are the short-range and long-range parts of the correlation-polarization potential. r_c is the outermost point, at which $V_{\rm pol}$ becomes larger than $V_{\rm corr}$. $V_{\rm corr}$ is based on the functional $\epsilon^{e-p}[\rho(\mathbf{r}_{\rm e}|\mathbf{R})]$ for the correlation energy of one positron in an electron gas with density $\rho(\mathbf{r}_{\rm e}|\mathbf{R})$. Boronski and Nieminen [38] have derived interpolation formulae for ϵ^{e-p}. $V_{\rm corr}$ can be obtained from ϵ^{e-p} by the functional derivative [32]

$$V_{\rm corr}(\mathbf{r}_p|\mathbf{R}) = \frac{\delta}{\delta\rho}\left\{\epsilon^{e-p}[\rho(\mathbf{r}_p|\mathbf{R})]\right\}. \tag{23}$$

The long-range part $V_{\rm pol}$ of the correlation-polarization potential is given by

$$V_{\rm pol}(\mathbf{r}_p|\mathbf{R}) = -\frac{1}{2r_p^6}\sum_{ij} x_i x_j \alpha_{ij}, \tag{24}$$

where α_{ij} are the Cartesian elements of the polarizability tensor, $r_p = |\mathbf{r}_p| = \sqrt{\sum_i x_i^2}$ and $x_i,\ x_j \in \{x, y, z\}$ are the Cartesian coordinates of the positron.

2.3 Cross sections for vibrational excitation

We are further including inelastic effects by describing the vibrationally inelastic cross section by the first Born dipole approximation, see e.g. Lane [39] for more details. The total inelastic cross section for vibrational excitation is given by the sum

$$\sigma_{\rm vib} = \sum_{\nu} \sigma_{\nu}^{\rm vib}. \tag{25}$$

Each partial excitation cross section $\sigma_{\nu}^{\rm vib}$ for the excitation of the vibrational mode ν is expressed as [39]

$$\sigma_{\nu}^{\rm vib} = \frac{8\pi}{3k^2} M_{\nu}^2 \ln\left|\frac{k + k'_{\nu}}{k - k'_{\nu}}\right|, \tag{26}$$

where we have used atomic units. The quantities

$$k = \sqrt{2E_{\rm scat}} \quad \text{and} \quad k'_{\nu} = \sqrt{2(E_{\rm scat} - E_{\nu})} \tag{27}$$

are the momenta of the positron before and after the collision, respectively. $E_{\rm scat}$ is the collision energy of the impinging particle, E_{ν} is the energy for exciting the vibrational mode ν and M_{ν} is the value of the transition dipole moment. The square of the transition dipole moment can be computed from the intensity of the infrared absorption by [40]

$$M_{\nu}^2 = \frac{A_{\nu}}{16.192\omega_{\nu}}, \tag{28}$$

where A_{ν} is the infrared absorbtion intensity, given in km mol^{-1}, and ω_{ν} is the frequency of the mode given in cm^{-1}. Both quantities can be computed with many standard quantum chemistry packages as e.g. Gaussian [41].

Similarly the expression for the total differential cross section (DCS) for vibrational excitation can be given by the sum

$$\frac{{\rm d}\sigma_{vib}}{{\rm d}\Omega} = \sum_{\nu} \frac{{\rm d}\sigma_{\nu}^{\rm vib}}{{\rm d}\Omega}, \tag{29}$$

where each mode contributes the partial DCS

$$\frac{{\rm d}\sigma_{\nu}^{\rm vib}}{{\rm d}\Omega} = \frac{4k'_{\nu}}{3k} \frac{M_{\nu}^2}{k^2 + k'^2_{\nu} - 2kk'_{\nu}\cos\theta}. \tag{30}$$

Here θ is the scattering angle.

2.4 Computational details

The equilibrium geometry of the uracil molecule belongs to the C_s symmetry. The molecular geometry and the ground state molecular orbitals are generated with the Gaussian 09 program package employing the Perdew-Burke-Ernzerhof (PBE) density functional and the aug-cc-pVTZ basis set [41]. The computed molecular dipole moment at this level of theory is 4.34 Debye, which compares well with the value of 4.38 Debye computed by Pluta et al. [33] using the analytic response coupled cluster singles doubles (CCSD) method and the aug-cc-pVTZ basis set. Brown et al. [34] have derived a value

Table 1. Vibrational frequencies ω_ν and infrared absorption intensities A_ν computed with the PBE density functional and the aug-cc-pVTZ basis set using the program package Gaussian [41].

Mode ν	Symmetry	$\frac{\omega_\nu}{\mathrm{cm}^{-1}}$	$\frac{A_\nu}{\mathrm{km\ mol}^{-1}}$
1	A″	145.5549	1.7483
2	A″	165.4788	0.0214
3	A′	371.9560	18.0256
4	A″	391.7149	19.9442
5	A′	502.8385	19.3562
6	A′	522.3072	6.3329
7	A′	539.5588	3.6425
8	A″	569.6779	36.0947
9	A″	675.7517	63.1804
10	A″	710.9749	16.5865
11	A″	737.7973	29.8373
12	A′	750.9808	2.7455
13	A″	797.4612	52.7301
14	A′	935.1604	9.4012
15	A″	940.1599	0.1702
16	A′	962.7717	6.1939
17	A′	1058.2382	3.9031
18	A′	1153.2323	88.0490
19	A′	1191.8136	6.3770
20	A′	1328.1998	20.6110
21	A′	1354.3773	82.3527
22	A′	1371.0682	15.2428
23	A′	1451.3918	79.1906
24	A′	1621.4944	51.7682
25	A′	1706.3841	642.5709
26	A′	1745.5493	570.7372
27	A′	3127.0491	2.8009
28	A′	3175.4055	1.1888
29	A′	3505.5873	55.0670
30	A′	3552.2516	92.3301

of 3.87 Debye from the microwave spectrum of uracil-molecules embedded in expanded argon beams. They give a 10 percent error for their value. Kulakowski et al. [35] have measured 4.16 Debye for uracil in dioxane solutions. Our computed rotational constants are $A = 3.86$ GHz, $B = 1.99$ GHz and $C = 1.31$ GHz, which is in good agreement with the microwave results of Brown et al. [34]: 3.88, 2.02 and 1.33 GHz. The diagonal elements of the polarizability tensor, computed with the PBE-functional, are $\alpha_{xx} = 97.9$ bohr^3, $\alpha_{yy} = 80.3$ bohr^3 and $\alpha_{zz} = 42.4$ bohr^3. The off-diagonal element in the molecular plane is $\alpha_{xy} = 2.38$ bohr^3. This is in good agreement with the CCSD results of Pluta et al. [33] ($\alpha_{xx} = 96.6$ bohr^3, $\alpha_{yy} = 75.5$ bohr^3 and $\alpha_{zz} = 42.2$ bohr^3). The computation of the vibrational frequencies and infrared absorption intensities has been done at the same level of theory. The values are given in Table 1.

The single-centre-expansions of the molecular electron density and of the potential are done with an improved version of the SCELib3.0 computational library [42], to which we have added the correlation-polarization potential specific for modeling the interactions of the molecular electrons with slow positrons. The coupled scattering equations are solved by Volterra integration, using a recent implementation of the VOLSCAT program package [43]. More specifically the VOLSCAT suite of codes computes the integral cross section in the BF-frame (denoted previously as σ_{cc}) and therefore generates the necessary body-fixed **K**-matrices.

Table 2. Computed partial integral cross sections. Energies are given in eV and all cross section are given in 10^{-16} cm^2.

Energy ν	$\sigma_{00}^{\mathrm{rot}}$	$\sigma_{01}^{\mathrm{rot}}$	$\sigma_{02}^{\mathrm{rot}}$	$\sigma_{03}^{\mathrm{rot}}$	$\sigma_{04}^{\mathrm{rot}}$
1.0	24.6	1132.2	18.8	16.2	19.5
1.5	18.7	779.3	10.9	10.8	13.8
2.0	16.4	597.4	7.9	8.0	10.5
2.5	15.0	485.6	6.6	6.4	8.3
3.0	14.0	410.3	6.0	5.3	6.9
3.5	13.2	355.6	5.7	4.5	6.0
4.5	12.0	281.4	5.4	3.6	4.9
5.0	11.6	255.0	5.3	3.3	4.6
6.0	10.8	215.3	5.1	3.0	4.3
8.0	9.7	164.9	4.5	2.5	4.0
10.0	9.1	133.5	3.9	2.3	3.8
12.0	8.7	113.0	3.4	2.0	3.6
14.0	8.5	98.4	2.9	1.8	3.4
16.0	8.3	86.5	2.5	1.6	3.2
18.0	8.1	77.3	2.2	1.5	3.0
20.0	7.9	70.7	1.9	1.4	2.8
25.0	7.3	57.8	1.4	1.3	2.4

The body-fixed **K**-matrices are then processed by the program package POLYDCS [36], that transforms the body-fixed **K**-matrices into the space-fixed **K**-matrices and further applies the Born correction, as outlined by Sanna and Gianturco [36]. From the space-fixed **K**-matrices obtained in this way we can further generate the state-to-state rotationally elastic and inelastic differential and integral cross sections. During the frame transformation step of the present calculations the rotational eigenfunctions and eigenvalues for the asymmetric top are in turn generated using the program ASYMTOP of Jain and Thompson [44] with our computed rotational constants. The convergence of scattering wavefunction with respect to the size of the partial wave expansion is checked carefully. The scattering wavefunction is expanded up to $L_{\max} = 40$. The actual expansion of the potentials in these calculations is done up to an angular momentum twice as large as the one which we used for the scattering wavefunctions (i.e. $2 \times L_{\max}$).

3 Results and discussion

As mentioned in the introduction, the scattering of positrons from molecular gases is a process involving a somewhat more varied ensemble of the system's responses to this projectile in comparison with the same experiments with an electron as a projectile.

One of the basic questions, for instance, is to be able to verify through computational models what is the expected size of the elastic integral cross sections caused by

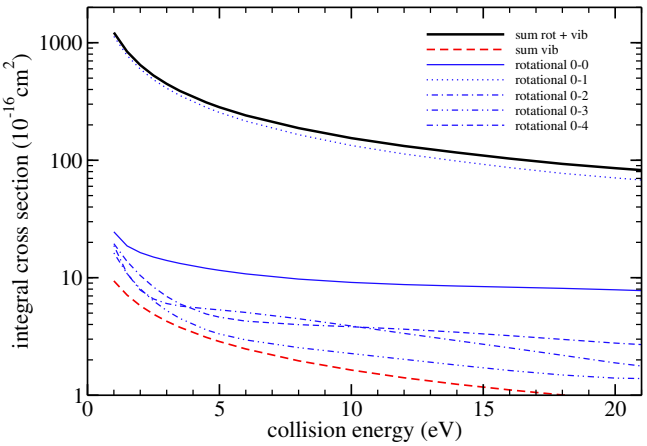

Fig. 1. Comparison of partial integral cross sections. The thin blue lines show the various contributions to the rotational elastic (rotational 0–0, thin solid blue line) and inelastic cross sections (other thin blue lines). The sum of the all vibrational inelastic cross sections is shown by the thick dashed red line. The sum of rotational elastic and inelastic and vibrational inelastic cross sections is shown by the solid black line.

Table 3. Computed partial integral cross sections. Energies are given in eV and all cross section are given in 10^{-16} cm^2.

Energy ν	$\sigma_{\rm rot}$	$\sigma_{\rm vib}$	$\sigma_{\rm rot}+\sigma_{\rm vib}$
1.0	1211.3	9.4	1220.7
1.5	833.4	7.1	840.5
2.0	640.1	5.8	645.9
2.5	521.9	4.9	526.8
3.0	442.6	4.3	446.8
3.5	385.1	3.8	388.8
4.5	307.4	3.1	310.5
5.0	279.8	2.9	282.7
6.0	238.3	2.5	240.8
8.0	185.7	2.0	187.6
10.0	152.6	1.6	154.2
12.0	130.8	1.4	132.2
14.0	115.1	1.2	116.3
16.0	102.2	1.1	103.3
18.0	92.1	1.0	93.1
20.0	84.7	0.9	85.6
25.0	70.2	0.8	71.0

positron scattering *vis-à-vis* the same process with electrons. In an earlier study comparing angular distributions for electron and positron scattering off the C_2H_2 molecule, for instance, the authors found the positron angular distributions, hence the corresponding ICS, to be smaller than those caused by electrons, apart from a small angular cone in the forward direction [28]. One further aspect of the experimental detection of integral cross sections is the difficulty, for polar molecules, to reliably evaluate the scattered positron distribution in the forward direction and at low energies. Hence, the discussion outlined below.

Our computed partial integral cross sections are shown in Figure 1 and compared with each other in terms of relative sizes. In the energy range considered the rotational

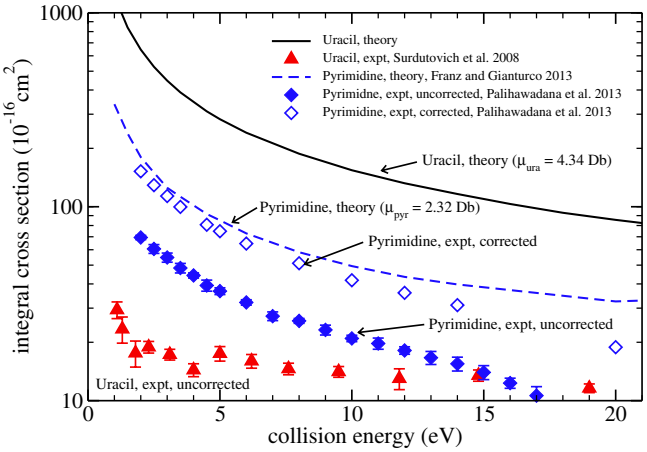

Fig. 2. The computed elastic integral cross sections for positron scattering from uracil is shown for the maximum angular expansion $L_{\rm max} = 40$ by the solid black line. For comparison our computed elastic integral cross sections for positron scattering from pyrimidine [37] is also shown (dashed blue line). The experimental data for positron uracil scattering by Surdutovich et al. [16] is given by the upwards red triangles. For comparison the experimental data for positron scattering from pyrimidine by Palihawadana et al. [17] is also shown (raw data: full blue diamonds, data including computed corrections for the forward scattering: open blue diamonds).

inelastic cross section from $J = 0$ to $J' = 1$ is dominant. It is more than one order of magnitude larger than the rotational elastic cross section and more than two orders of magnitude larger than the sum of the vibrational inelastic cross sections.

For comparison we also report in Figure 2 the ICS for uracil with those of the pyrimidine molecule, which we recently studied with similar calculations [37]. Note that the pyrimidine ICS includes rotational elastic and inelastic channels only, whereas the uracil ICS additionally includes the vibrationally inelastic channels. They seem to be much smaller in size than those calculated for uracil, and also to agree with the corresponding experiment on this molecule [37]. The set of experimental data for positron-uracil scattering is also shown in Figure 2. The red upwards triangles are the experiments published by Surdutovich et al. [16]. Due to the limited energy resolution in this experiments the measured cross sections includes rotationally and vibrationally elastic and inelastic processes.

The following comments could be made by looking at the data reported in the figure: One is naturally aware that, when doing scattering of positrons and electrons off gaseous molecular targets with permanent dipole moments, the use of a body-fixed reference frame produces divergent behavior of the angular distributions in the forward direction, hence the corresponding elastic ICS turn out to be incorrect chiefly in the small energy range where forward scattering is usually dominant. One would therefore need to go through the calculations of the corresponding differential cross sections, modifying them for the higher angular momentum contributions via the Born

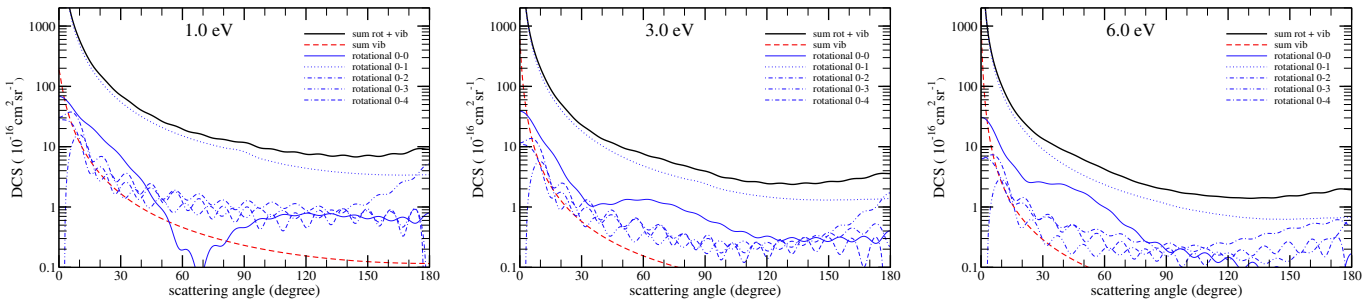

Fig. 3. Comparison of partial differential cross sections at collision energies of 1.0 eV (left panel), 3.0 eV (middle panel) and 6.0 eV (right panel). The thin blue lines show the various contributions to the rotational elastic (rotational 0–0, thin solid blue line) and inelastic cross sections (other thin blue lines). The sum of the all vibrational inelastic cross sections is shown by the thick dashed red line. The sum of rotational elastic and inelastic and vibrational inelastic cross sections is shown by the solid black line.

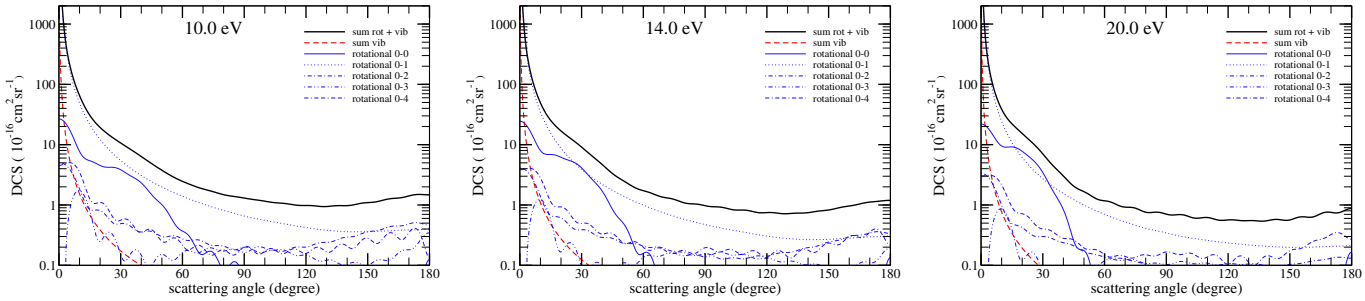

Fig. 4. Same as Figure 3, but for collision energies of 10.0 eV (left panel), 14.0 eV (middle panel) and 20.0 eV (right panel).

correction [29]. Therefore, although the present experimental data do not cover the small angle region accurately nor manage to go down to very low scattering energies, we still expect that the corrections to the final cross sections outlined in the previous discussion of our approach, and carried out here by us, should have for this system the same dramatic effect of correcting the low-energy, forward scattering distributions as that observed earlier for another, albeit less polar, similar system: gas-phase pyrimidine [37].

To further analyze this point, we also report in Figure 2 the sequence of the forward correction effects on pyrimidine, already discussed in our earlier work on this system [37]. The set of data given by the figure refers to the data by Palihawadana et al. [17]. The experiments by Palihawadana et al. is employing a linear transmission technique. In such experiments unscattered particles cannot be distinguished from particles that are scattered by an angle lower than the angular discrimination angle $\theta_{\min}$, see e.g. Sullivan et al. [45]. This angle can be estimated by a function of the retarding potential and of the scattering energy, as suggested by Kauppila et al. [46] and Kwan et al. [47]. The uncorrected data points of Palihawadana et al. [17] are given by the solid blue diamonds. We have added to these points the integral of our computed differential cross section for the forward-scattering cone between the forward direction and the angular discrimination angle $\theta_{\min}$, as described in detail in reference [37]. The corrected experimental data are given by the open blue diamonds. One clearly sees that the more realistic inclusion of forward scattering data in the evaluation of the ICS produces over the whole range of energies a marked increase of the sizes, with an even more dramatic change at energies below about 7–8 eV: at 3 eV, for instance, the pyrimidine ICS value changes from about 40 Å^2 to more than 120 Å^2! Thus, it is reasonable to expect that the similar set of corrections, when applied to the uncorrected ICS of uracil of Surdutovich et al. [16], could lead to an increase close to almost 400 Å^2, not far from the computed value where the effect of the long-range dipole has also been correctly included at all angles, as outlined before. Furthermore, we see that the ICS data of both uracil and pyrimidine are strongly controlled by dipole scattering: in fact, we see in Figure 2 that to go from a system with a permanent dipole of $\mu \approx 2.3$ Debye, to one with $\mu \approx 4.3$ Debye causes the corresponding ICS to nearly quadruple in value, as expected, given the influence of the quadratic dipole term in the Born approximation.

Our computed partial differential cross sections at various scattering energies are shown in Figures 3 and 4 and are listed for some selected energies, and for some representative scattering angles, in Tables 4 and 5. All cross sections have strong forward peaks, due to the dipole term in the rotational inelastic cross section for the $J = 0$ to $J' = 1$ transition. The sum of the vibrational inelastic cross sections have a very narrow forward scattering peak due to the transition dipole moment of the various vibrational excitations. These figures show clearly that most of the contributions to the scattering cross sections are contained in a small forward cone.

Table 4. Various contributions to the DCS at collision energies of 1.0 eV (left), 3.0 eV (middle) and 6.0 eV (right). All values are given in 10^{-16} cm^2 sr^{-1}.

Energy	1.0 eV					3.0 eV					6.0 eV				
Angle	30	60	90	120	150	30	60	90	120	150	30	60	90	120	150
$\frac{d\sigma_{elas}}{d\Omega}$	7.0	0.2	0.5	0.8	0.6	1.5	1.3	0.6	0.3	0.3	2.6	1.0	0.2	0.1	0.1
$\frac{d\sigma_{rot}}{d\Omega}$	69.3	19.2	11.5	7.3	7.1	22.3	7.4	3.9	2.4	2.6	13.2	4.2	1.9	1.4	1.5
$\frac{d\sigma_{vib}}{d\Omega}$	1.7	0.5	0.2	0.2	0.1	0.6	0.2	0.1	0.1	0.0	0.3	0.1	0.0	0.0	0.0
$\frac{d\sigma_{rot}}{d\Omega} + \frac{d\sigma_{vib}}{d\Omega}$	71.0	19.6	11.8	7.5	7.2	22.9	7.6	3.9	2.4	2.6	13.5	4.2	2.0	1.4	1.5

Table 5. Various contributions to the DCS at collision energies of 10.0 eV (left), 14.0 eV (middle) and 20.0 eV (right). All values are given in 10^{-16} cm^2 sr^{-1}.

Energy	10.0 eV					14.0 eV					20.0 eV				
Angle	30	60	90	120	150	30	60	90	120	150	30	60	90	120	150
$\frac{d\sigma_{elas}}{d\Omega}$	3.8	0.4	0.1	0.0	0.0	4.1	0.2	0.0	0.0	0.0	3.4	0.0	0.0	0.0	0.0
$\frac{d\sigma_{rot}}{d\Omega}$	10.5	2.4	1.3	1.0	1.1	9.0	1.7	1.0	0.7	0.8	7.0	1.2	0.7	0.6	0.6
$\frac{d\sigma_{vib}}{d\Omega}$	0.2	0.0	0.0	0.0	0.0	0.1	0.0	0.0	0.0	0.0	0.1	0.0	0.0	0.0	0.0
$\frac{d\sigma_{rot}}{d\Omega} + \frac{d\sigma_{vib}}{d\Omega}$	10.7	2.5	1.3	1.0	1.1	9.1	1.7	1.0	0.7	0.8	7.0	1.2	0.7	0.6	0.6

4 Present conclusions

The interaction of slow positrons with biosystems at low scattering energies are of current interest in that they can provide information on the structural issues related to the positron physics of these systems, thereby answering questions such as:

1. How large are the integral cross sections for the RNA and DNA and its components in relation to the behavior of low-energy electrons?
2. Can we estimate the annihilation efficiency of the above molecules, thereby relating such data, which are molecule-specific, to the necessary sensitivity of tomographic analysis?

In the present study we have started to work on a computational answer to the first of the above questions and have provided a realistic estimate, starting from first principles and carrying out accurate, multichannel scattering calculations, of the elastic integral cross sections for the uracil molecule in the gas phase, further correcting the computed data for the overall effect of the permanent dipole moment of the target, as discussed earlier.

In relation to the existing experiments, our data indicate thus far that the average size of the computed cross sections in comparison with the available measurements is much larger than the latter and shows a much stronger increase at threshold.

In order to better understand the reliability of such findings, we have looked at the same calculations for the pyrimidine molecules, for which a larger group of experiments is available and which have been shown by our earlier comparison between them [37] to be in very good accord with each other, as shown again by the data in Figure 2. Additionally, when we further detail the comparison between the two sets of calculations (see Fig. 2) it shows that, as expected, the ICS data for uracil are much larger and go more rapidly to larger values as the energy decreases. As a matter of fact, we have argued in our previous discussion that both sets of cross sections are dominated by dipole-driven interaction and therefore since the uracil system has nearly twice as large a dipole, the corresponding ICS below 10 eV of collision energy should accordingly increase by a factor of four, as indeed seen to occur in our calculations as reported in that figure.

Given the further observation that our computed pyrimidine cross sections are in very good accord, both in size and energy dependence, with the corrected experimental data, and that the experiments for the latter molecule appear in Figure 2 to be larger than the existing experiments for uracil, we surmise that our converged calculations for integral cross sections presented in this work indicate rather convincingly that the experimental data may still be missing a substantial cone of positron flux in the forward directions for the lower collision energies. To further provide helpful comparison data to future experiments, we also report in several figures and in detailed tables the angular scattering of positron projectiles from gas-phase uracil molecules.

In conclusion, the present discussion on our new calculations for the uracil molecule and our further comparison of these ICS with the earlier data for pyrimidine [37], suggests that the former target gas should exhibit much larger integral cross section values from experiments in the low-energy regions and that the calculations already indicate such an increase with respect to both the existing experiments and the similar data for another polar gas with a much smaller permanent dipole moment: pyrimidine.

This work was carried out under the HPC-EUROPA2 project (Project Number: 228398) with the support of the European

Commission Capacities Area – Research Infrastructures Initiative. It has also been supported by the COST Action MP 1002 – Nano-scale Insights into Ion Beam Cancer Therapy (Nano-IBCT). The additional support of CINECA computational grants is gratefully acknowledged. J.F. thanks the staff at CINECA for their kind hospitality and support. We thank Sergio Orlandini, Mario Tacconi and Nico Sanna of CINECA for maintaining the SCELib software package.

References

1. A.L. Lehninger, *Biochemistry* (Worth, New York, 1970)
2. B.D. Michall, P.A. O'Neil, Science **287**, 1603 (2000)
3. B. Boudaiffa, P. Clouthier, D. Hunting, M.A. Huels, L. Sanche, Science **287**, 1658 (2000)
4. I. Baccarelli, I. Bald, F.A. Gianturco, E. Illenberger, J. Kopyra, Phys. Rep. **508**, 1 (2011)
5. S. Denifl, S. Ptasinska, M. Probst, J. Hrusak, P. Scheier, T.D. Märk, J. Phys. Chem. A **108**, 6562 (2004)
6. F.A. Gianturco, R.R. Lucchese, J. Chem. Phys. **120**, 7446 (2004)
7. S. Ptasinska, S. Denifl, P. Scheier, E. Illenberger, T.D. Märk, Angew. Chem. Int. Ed. **44**, 1647 (2005)
8. J. Simons, Acc. Chem. Res. **39**, 772 (2006)
9. M. Charlton, J.W. Humberston, *Positron Physics* (Cambridge University Press, Cambridge, 2001)
10. *New Directions in Antimatter Chemistry and Physics*, edited by C.M. Surko, F.A. Gianturco (Kluwer Academic Publishers, Dordrecht, 2001)
11. F.A. Gianturco, T.L. Gibson, P. Nichols, R.R. Lucchese, T. Nishimura, Radiat. Phys. Chem. **68**, 673 (2003)
12. J. Franz, F.A. Gianturco, Nucl. Instrum. Methods Phys. Res. B **247**, 20 (2006)
13. R. Zhang, K.L. Baluja, J. Franz, J. Tennyson, J. Phys. B **44**, 035203 (2011)
14. C.M. Surko, G.F. Gribakin, S.J. Buckman, J. Phys. B **38**, R57 (2005)
15. G.F. Gribakin, J.A. Young, C.M. Surko, Rev. Mod. Phys. **82**, 2557 (2010)
16. E. Surdutovich, G. Setzler, W.E. Kauppila, S.J. Rehse, T.S. Stein, Phys. Rev. A **77**, 054701 (2008)
17. P. Palihawadana, R. Boadle, L. Chiari, E.K. Anderson, J.R. Machacek, M.J. Brunger, S.J. Buckman, J.P. Sullivan, Phys. Rev. A **88**, 012717 (2013)
18. F.A. Gianturco, R. Melissa, Phys. Rev. A **54**, 357 (1996)
19. F.A. Gianturco, R. Melissa, Nucl. Instrum. Methods Phys. Res. B **143**, 81 (1998)
20. F.A. Gianturco, R. Melissa, J. Phys. B **29**, L719 (1996)
21. K.L. Baluja, A. Jain, Phys. Rev. A **75**, 7838 (1992)
22. D.D. Reid, J.M. Wadehra, J. Phys. B **29**, L127 (1996)
23. D.D. Reid, J.M. Wadehra, J. Phys. B **30**, 2318 (1997)
24. L. Chiari, A. Zecca, S. Girardi, E. Trainotti, G. Garcia, F. Blanco, R.P. McEachran, M.J. Brunger, J. Phys. B **45**, 215206 (2012)
25. S. Denifl, B. Sonnweber, G. Hanel, P. Scheier, T.D. Märk, Int. J. Mass Spectrom. **238**, 47 (2004)
26. S.D. Wetmore, R.J. Boyd, L.A. Eriksson, Chem. Phys. Lett. **343**, 151 (2001)
27. J.W. Humberston, P. Van Reeth, M.S.T. Watts, W.E. Meyerhof, J. Phys. B **30**, 2477 (1997)
28. J. Franz, F.A. Gianturco, K.L. Baluja, J. Tennyson, R. Carey, R. Montuoro, R.R. Lucchese, T. Stoecklin, P. Nicholas, T.L. Gibson, Nucl. Instrum. Methods Phys. Res. B **266**, 425 (2008)
29. F.A. Gianturco, A. Jain, Phys. Rep. **143**, 347 (1986)
30. E.S. Chang, U. Fano, Phys. Rev. A **6**, 173 (1972)
31. R. Curik, F.A. Gianturco, N. Sanna, J. Phys. B **33**, 2705 (2000)
32. A. Jain, F.A. Gianturco, J. Phys. B **24**, 2387 (1991)
33. T. Pluta, M. Kolaski, M. Medved, S. Budzak, Chem. Phys. Lett. **546**, 24 (2012)
34. R.D. Brown, P.D. Godfrey, D. McNaughton, A.P. Pierlot, J. Am. Chem. Soc. **110**, 2330 (1988)
35. I. Kulakowski, M. Geller, B. Lesyng, K.L. Weirzchowski, Biochem. Biophys. Acta **361**, 119 (1974)
36. N. Sanna, F.A. Gianturco, Comput. Phys. Commun. **114**, 142 (1998)
37. J. Franz, F.A. Gianturco, Phys. Rev. A **88**, 042711 (2013)
38. E. Boronski, R.M. Nieminen, Phys. Rev. **34**, 3820 (1986)
39. N.F. Lane, Rev. Mod. Phys. **52**, 29 (1980)
40. D.J. Swanton, G.B. Bacskay, N.S. Hush, J. Chem. Phys. **84**, 5715 (1986)
41. M.J. Frisch et al., *Gaussian 09*, Revision B.01 (Gaussian Inc., Wallingford CT, 2010)
42. N. Sanna, I. Baccarelli, G. Morelli, Comput. Phys. Commun. **180**, 2544 (2009)
43. N. Sanna, I. Baccarelli, G. Morelli, Comput. Phys. Commun. **180**, 2550 (2009)
44. A. Jain, D.G. Thompson, Comput. Phys. Commun. **32**, 367 (1984)
45. J.P. Sullivan, C. Makochekanwa, A. Jones, P. Caradonna, D.S. Slaughter, J. Machacek, R.P. McEachran, D.W. Mueller, S.J. Buckman, J. Phys. B **44**, 035201 (2011)
46. W.E. Kauppila, T.S. Stein, J.H. Smart, M.S. Dababneh, Y.K. Ho, J.P. Downing, V. Pol, Phys. Rev. A **24**, 725 (1981)
47. C.K. Kwan, W.E. Kauppila, R.A. Lukaszew, S.P. Parikh, T.S. Stein, Y.J. Wan, M.S. Dababneh, Phys. Rev. A **44**, 1620 (1991)